



## Full Length Article

# Dilute long period stacking/order (LPSO)-variant phases along the composition gradient in a Mg-Ho-Cu alloy

Kai Guan<sup>a,\*</sup>, Daisuke Egusa<sup>a</sup>, Eiji Abe<sup>a,b,\*</sup><sup>a</sup>Department of Materials Science and Engineering, The University of Tokyo, Tokyo 113-8656, Japan<sup>b</sup>Research Center for Structural Materials, National Institute for Materials Science, Tsukuba 305-0047, Japan

Received 13 July 2021; received in revised form 13 October 2021; accepted 5 November 2021

Available online 10 December 2021

## Abstract

We have systematically investigated the microstructures of as-cast  $\text{Mg}_{97.49}\text{Ho}_{1.99}\text{Cu}_{0.43}\text{Zr}_{0.09}$  alloy by atomic resolution high-angle annular dark field scanning transmission electron microscopy (HAADF-STEM), revealing the coexistence of 18R, 14H and 24R long period stacking/order (LPSO) phases with fully coherent interfaces along step-like composition gradient in a blocky intermetallic compound distributed at grain boundary. The short-range order (SRO)  $\text{L}_{12}$ -type  $\text{Cu}_6\text{Ho}_8$  clusters embedded across AB'C'A-stacking fault layers are directly revealed at atomic scale. Importantly, the order degree of SRO clusters in the present dilute alloy is significant lower than previous 6M and 7M in-plane order reported in ternary Mg-TM (transition metal)-RE (rare earth) alloys, which can be well matched by 9M in-plane order. This directly demonstrates that SRO in-plane  $\text{L}_{12}$ -type clusters can be expanded into more dilute composition regions bounded along the definite TM/RE ratio of 3/4. In addition, the estimated chemical compositions of solute enriched stacking fault (SESF) in all LPSO variants are almost identical with the ideal SESF composition of 9M in-plane order, regardless of the type of LPSO phases. The results further support the viewpoint that robust  $\text{L}_{12}$ -type  $\text{TM}_6\text{RE}_8$  clusters play an important role in governing LPSO phase formation.

© 2021 Chongqing University. Publishing services provided by Elsevier B.V. on behalf of KeAi Communications Co. Ltd.

This is an open access article under the CC BY-NC-ND license (<http://creativecommons.org/licenses/by-nc-nd/4.0/>)

Peer review under responsibility of Chongqing University

**Keywords:** Magnesium alloys; Long period stacking/order (LPSO) phases; Short-range order (SRO) clusters; High-angle annular dark field scanning transmission electron microscopy (HAADF-STEM).

## 1. Introduction

As a light-weight structural metallic material, Mg alloy owning high specific strength shows great application prospect in automotive and aerospace industries. Nevertheless, its practical application is gravely restricted by the relatively low strength and poor ductility. Rare earth (RE) elements are recognized to be the significantly efficient alloying elements to optimize Mg alloys' mechanical properties [1–16]. Especially Mg-RE-TM (transition metal) ternary alloys containing long

period stacking/order (LPSO) phases have received considerable attention due to a good combination of strength and ductility [6–14]. The predominant strengthening mechanism was attributed to the formation of kink band, which can not only improve the yield strength significantly by inhibiting dislocation motion but also enhance the ductility effectively by accommodating the strain originating from applied stress during the plastic deformation [7–11].

In the past decades, great efforts have been made to develop high performance LPSO-containing Mg alloys. Five types of LPSO phases (12R, 10H, 14H, 18R and 24R) constructed by hexagonal close-packed (hcp) Mg layers and face-centered cubic (fcc) intrinsic-II type stacking faults ( $I_2$ -SF, AB'C'A-type stacking sequence) have been identified in ternary Mg-RE-TM alloys [17–28]. It was demonstrated that Y/Zn atoms segregated in the four successive atomic layers of AB'C'A building units in Mg-Zn-Y alloys would form robust

\* Corresponding author at: Department of Materials Science and Engineering, The University of Tokyo, Tokyo 113-8656, Japan.

\* Corresponding author at: Department of Materials Science and Engineering, The University of Tokyo, Tokyo 113-8656, Japan.

E-mail addresses: [guanikai129@163.com](mailto:guanikai129@163.com) (K. Guan), [abe@material.t.u-tokyo.ac.jp](mailto:abe@material.t.u-tokyo.ac.jp) (E. Abe).

$L_{12}$ -type  $Zn_6Y_8$  clusters with short range order (SRO) [20–22], which are believed to play an important role in enhancing the thermodynamic stability of LPSO phases through reducing the total Gibbs energy [29,30]. Similar  $L_{12}$ -type  $Al_6Gd_8$  clusters with long range order were also observed in 18R LPSO phase of a heat treated Mg-Al-Gd alloy [31]. As for an annealed Mg-Zn-Gd alloy, SRO  $L_{12}$ -type  $Zn_6Gd_8$  clusters were revealed in an isolated solute enriched stacking fault (SESF) in addition to LPSO phase [32]. More interestingly,  $D0_{19}$ -like  $ZnGd_3$  clusters were identified in the Mg matrix by means of atomic-resolution high-angle annular dark field scanning transmission electron microscopy (HAADF-STEM) and first-principles calculations, which are considered as precursors of SRO  $L_{12}$ -type  $Zn_6Gd_8$  clusters. Such precursor phenomenon was also demonstrated in Mg-Zn-Y and Mg-Zn-Gd systems by *in-situ* synchrotron radiation [33,34] and photoemission spectroscopy [35], suggesting SRO clusters first formed during the formation process of LPSO phases. First-principles calculations as well as scanning tunneling microscopy experiments predicted that the density of  $L_{12}$ -type clusters depends mainly on the composition of LPSO phase [36,37]. This was directly verified by diffraction pattern and atomic-resolution HAADF-STEM image recently. In that work [25],  $7M$  ( $7 \times (11\bar{2}0)_{hcp}$ ) in-plane order  $L_{12}$ -type clusters were observed in 12R LPSO phase for  $Mg_{79}Ni_9Y_{12}$  alloy, whose density is lower than that of  $6M$  ( $6 \times (11\bar{2}0)_{hcp}$ ) in-plane order clusters frequently observed in 10H, 14H and 18R LPSO phases for Mg-Zn-Y [20,21] and Mg-Al-Gd [31] alloys. Accordingly, the corresponding composition with non-stoichiometry extended into dilute solute range, but it was bounded along the definite Ni/Y ratio due to the formation of robust  $L_{12}$ -type clusters [25]. This suggests SRO clusters indeed play a key role in forming process of LPSO phase. In addition, 15R, 12H and 21R LPSO phases constructed by intrinsic- $I$  ( $I_I$ ) SFs with AB'C-type stacking sequence were definitely demonstrated in Mg-Co-Y [38] alloys using atomic-resolution HAADF-STEM. It should be noted that, similar to SRO  $L_{12}$ -type  $Zn_6Y_8$  clusters of  $I_2$ -type LPSO phase, SRO  $Co_3Y_5$  clusters embedded across the three consecutive atomic layers of  $I_I$  SFs were recently clarified in Mg-Co-Y alloys through the combination of atomic-resolution HAADF-STEM characterizations and density-functional theory (DFT) calculations [39].

Through the above analysis, it can be also deduced that TM may play a critical role in determining the type of LPSO structures in ternary Mg-TM-RE alloys. Cu is a typical TM element, its maximum solid solubility in Mg matrix is 0.013 at.%, which is much lower than 2.4 at.% of Zn [27]. It is worth noting that 18R LPSO phase was observed in the as-cast  $Mg_{97}Y_2Cu_1$  alloy and it could exist stably after heat treatment at 773 K for 10 h [27]. Additionally, the maximum solid solubility of Ho (5.44 at.%) in Mg matrix is larger than that of Gd (4.53 at.%) and Y (3.35 at.%), which can provide excellent solid solution strengthening and precipitation strengthening. Kawamura and Yamasaki [28] fabricated a series of  $Mg_{97}Zn_1RE_2$  (RE = La, Ce, Pr, Nd, Sm, Gd, Tb, Dy, Ho, Er, Tm, Yb and Y) alloys and observed the coexistence

of 18R and 14H LPSO phases in the as-cast  $Mg_{97}Zn_1Ho_2$  alloy. Remarkably, among of them,  $Mg_{97}Zn_1Ho_2$  alloy exhibited the best combination of strength and ductility at 473 K, its tensile yield strength reached to 310 MPa. This indicates that Ho indeed provides excellent strengthening effect, which can also be supported by other recent works [40,41]. On the basis of previous research, it is expected that the combination of Ho and Cu may be one of the promising candidates for the development of high performance Mg alloys. However, up to now, there has been no public report on Mg-Ho-Cu alloy. Although the LPSO formation in Mg-Ho-Cu alloy is predicted by DFT calculations [42], the experimental details, such as the type of LPSO phase and SRO cluster, and even cluster density still remain unrevealed.

In this work, the LPSO phases of the as-cast Mg-Ho-Cu-Zr alloy were thoroughly investigated using atomic-resolution HAADF-STEM. In particular, the blocky LPSO structural variants with coherent interfaces along the composition gradient were observed at grain boundary. The in-plane order cluster density is also discussed. Here, we should mention that a trace of Zr was added to refine grains.

## 2. Experimental procedures

The quaternary alloy with nominal composition of  $Mg_{97.5}Ho_{2.0}Cu_{0.4}Zr_{0.1}$  (at.%) was fabricated by melting high purity Mg, Cu, and Mg-Ho and Mg-Zr master alloys in an electrical resistance furnace. The melt was protected by the mixed atmosphere of 1%  $SF_6$  and 99%  $CO_2$  throughout the casting process until it was poured into a Cu-mold. The actual chemical composition of the present alloy was measured to be  $Mg_{97.49}Ho_{1.99}Cu_{0.43}Zr_{0.09}$  (at.%) by means of inductively coupled plasma atomic emission spectroscopy (ICP-AES). Microstructures were characterized by scanning electron microscope (SEM, JEOL JIB-4700F) equipped with energy-dispersive X-ray spectrometer (EDS, Oxford Instruments) under an accelerating voltage of 15 kV, transmission electron microscope (TEM, JEM-2010HC) with EDS operating at 200 kV and atomic-resolution aberration-corrected scanning transmission electron microscope (STEM, JEM-ARM200CF) operating at 200 kV. SEM-EDS test was carried out on an image with the magnification of 6 k, and the work distance was set as 8 mm. The corresponding EDS data was quantitatively analyzed by the software including ZAF corrections. For HAADF-STEM observations, we used convergence semi-angle of 22 mrad and high-angle annular dark field detector ranged from 68 mrad to obtain atomic number (Z)-contrast images. Thin foils for TEM/STEM observations were mechanically polished to about 25  $\mu m$ , and then ion-milled using precision ion polishing system (PIPS, Gatan 691) equipped with liquid nitrogen cooling system. Atomic-resolution HAADF-STEM image simulations were performed with the Dr. Probe software package [43]. The specimen thickness of about 20 nm was used in simulations, consistent with the thickness of experimental specimens. The probe was set to zero aberration. The acceleration voltage was set

Table 1.

The experimental chemical compositions of LPSO phases measured by SEM-EDS and the corresponding estimated SESFs compositions.

Region (LPSO)	LPSO compositions (wt.%)				SESF compositions (wt.%)		
	Cu	Ho	Zr	Mg	Cu	Ho	Mg
A(18R)	4.1	4.9	0.1	Balance	6.2	7.4	Balance
B(14H)	3.0	4.1	0.1	Balance	5.3	7.2	Balance
C(24R)	2.7	3.7	0.1	Balance	5.4	7.4	Balance

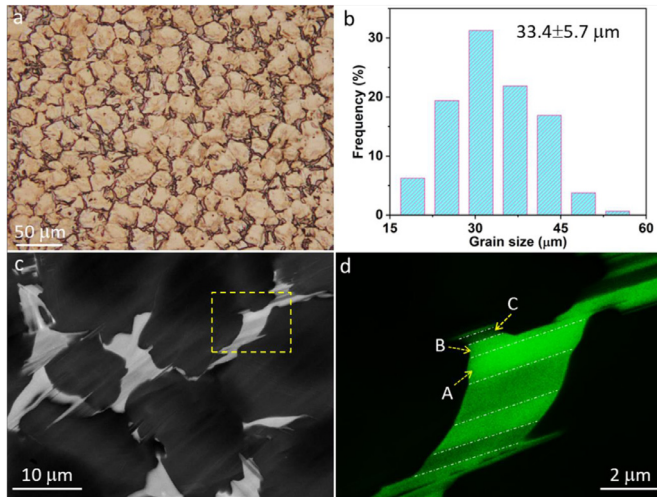


Fig. 1. The typical OM image (a) of as-cast  $\text{Mg}_{97.49}\text{Ho}_{1.99}\text{Cu}_{0.43}\text{Zr}_{0.09}$  alloy and the corresponding histogram of grain size (b), backscattered SEM image (c), and the enlarged image (d) recolored with green corresponding to the yellow dashed rectangle in (c) (For interpretation of the references to color in this figure, the reader is referred to the web version of this article.).

to 200 kV, and a convergence angle of 22 mrad was used, consistent with the experimental parameters. The inner and outer radii of the HAADF detector were set to 68 mrad and 120 mrad, respectively.

### 3. Results

The typical OM image of the as-cast  $\text{Mg}_{97.49}\text{Ho}_{1.99}\text{Cu}_{0.43}\text{Zr}_{0.09}$  alloy and the corresponding histogram of grain size distribution are shown in Fig. 1a and b, respectively. The average grain size is estimated to be  $33.4 \pm 5.7 \mu\text{m}$ , which is much smaller than that of other traditional as-cast Mg-TM-RE alloys [28]. Fig. 1c presents a representative backscattered SEM image. Numerous blocky intermetallic compounds with bright contrast are obviously distributed at grain boundaries. On closer inspection, the contrast distinction within the interior of a blocky phase at the grain boundary frequently occurs, which can be observed more clearly in the enlarged image (Fig. 1d) recolored with green corresponding to the region marked by yellow dashed rectangle in Fig. 1c. As shown in Table 1, the compositions of A, B and C regions indicated by yellow arrows in Fig. 1d are measured to be  $\text{Mg}_{90.9}\text{Ho}_{4.9}\text{Cu}_{4.1}\text{Zr}_{0.1}$ ,  $\text{Mg}_{92.8}\text{Ho}_{4.1}\text{Cu}_{3.0}\text{Zr}_{0.1}$ , and  $\text{Mg}_{93.5}\text{Ho}_{3.7}\text{Cu}_{2.7}\text{Zr}_{0.1}$ , respectively, by means of SEM-

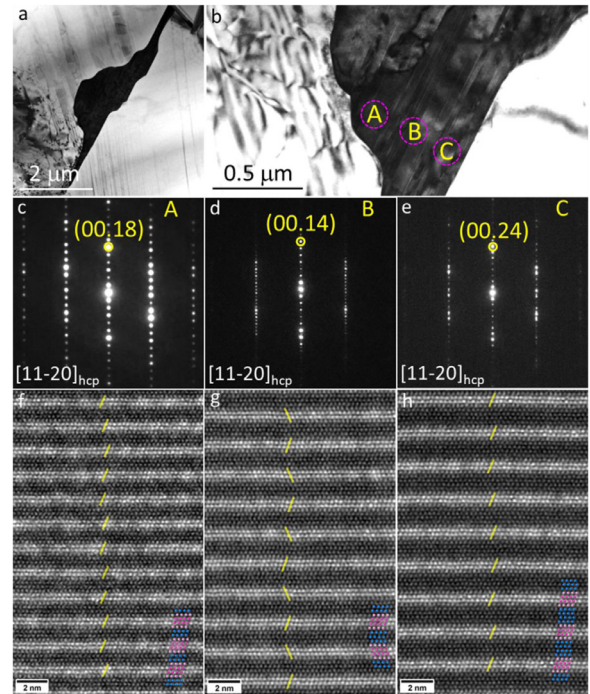


Fig. 2. Bright-field TEM images (a, b), SAED patterns (c–e) taken along  $[11\bar{2}0]_{\text{hcp}}$  and atomic-resolution HAADF-STEM images (f–h). (c, f), (d, g) and (e, h) correspond to A, B and C regions marked in (b), respectively. The corresponding structural models of LPSO variants are attached in (f–h), blue: Mg, dark pink and light pink: solute-enriched Mg sites with different degrees of solute occupations (For interpretation of the references to color in this figure, the reader is referred to the web version of this article.).

EDS. The distinctions of contrast and chemical composition imply the existence of variants with different crystalline structures in blocky phases.

In order to well identify the detailed structures of blocky phases, TEM and atomic-resolution HAADF-STEM characterizations were performed. Fig. 2a is the bright-field TEM image taken along  $[11\bar{2}0]_{\text{hcp}}$  zone axis of the blocky phase, in which plenty of lamellar structures subsequently identified as LPSO phases using STEM are observed in the interior of Mg grains. The high magnification image of local blocky phase is shown in Fig. 2b. Fig. 2c–e present the selected area electron diffraction (SAED) patterns taken along  $[11\bar{2}0]_{\text{hcp}}$  zone axes, which are corresponding to A, B and C regions marked by pink dotted circles in Fig. 2b, respectively. As shown in Fig. 2c, there are five extra diffraction spots distributed homogeneously between  $(0000)_{\text{hcp}}$  and  $(0002)_{\text{hcp}}$  spots, implying a superstructure containing six basic units in  $c^*$  direction, which

is similar to 12H and 18R LPSO phases. Due to the invisibility of  $(10\bar{1}0)_{\text{hcp}}$  spot, this phase can be determined as 18R LPSO phase with the lattice parameters of  $a = 0.321$  nm,  $c = 4.689$  nm. As shown in Fig. 2d, 14H and 21R LPSO structures are suggested by the even distribution of six extra diffraction spots between  $(0000)_{\text{hcp}}$  and  $(0002)_{\text{hcp}}$  spots. The relevant phase is finally identified as 14H LPSO structure ( $a = 0.321$  nm,  $c = 3.647$  nm) because of the existence of  $(10\bar{1}0)_{\text{hcp}}$  spot. In the same way, the SAED pattern with the uniform distribution of seven extra diffraction spots between  $(0000)_{\text{hcp}}$  and  $(0002)_{\text{hcp}}$  presented in Fig. 2e can be indexed as 24R LPSO phase ( $a = 0.321$  nm,  $c = 6.252$  nm). The typical atomic-resolution HAADF-STEM images obtained from A, B and C regions in Fig. 2b are presented in Fig. 2f–h, respectively. It can be seen that all three kinds of LPSO structures are constructed by Mg layers and AB'C'A building units with distinct segregation of Cu/Ho atoms. The numbers of Mg layers sandwiched between each two adjacent building units in Fig. 2f–h are 2, 3 and 4, respectively, directly vindicating the analysis results of SAED patterns. In addition, the even number (2 and 4) of the sandwiched Mg layers results in the same shear direction of the stacking sequences in each two adjacent building units for 18R and 24R LPSO phases, while the odd number (3) results in opposite shear directions for 14H LPSO phase, as highlighted by yellow bars in corresponding images. Further inspection of the HAADF-STEM images reveals that each four-layered building unit contains two inner layers with significant segregation and two outer layers with intermediate segregation, which is well consistent with previous results in Mg-Zn-RE alloys [17,20]. Structure models of 18R, 14H and 24R LPSO phases are inserted in the lower-right corner of Fig. 2f–h, where blue, dark pink and light pink circles represent *hcp* layer, *fcc* layer and *hcp* layer next to *fcc*, respectively. By using TEM-EDS, the compositions of A, B and C regions marked in Fig. 2b were measured to be  $\text{Mg}_{91.16}\text{Ho}_{4.76}\text{Cu}_{4.05}\text{Zr}_{0.03}$  (18R),  $\text{Mg}_{92.60}\text{Ho}_{4.27}\text{Cu}_{3.07}\text{Zr}_{0.06}$  (14H) and  $\text{Mg}_{93.22}\text{Ho}_{3.87}\text{Cu}_{2.85}\text{Zr}_{0.06}$  (24R), respectively. Combined with the SEM-EDS results, it can be inferred that A, B and C regions indicated in Fig. 1d correspond to 18R, 14H and 24 R LPSO phases, respectively.

Fig. 3a shows the low magnification HAADF-STEM image corresponding to Fig. 2a, its contrast feature seems like that in the backscattered SEM image shown in Fig. 1c. The high magnification HAADF-STEM image around the local region marked by pink rectangle in Fig. 3a are shown in Fig. 3b, whose white rectangle region is further enlarged in Fig. 3c, in which Z-contrast distinctions of the blocky phase are obviously observed and the boundaries are highlighted by azure dotted lines. The Z-contrast intensity profile obtained from the yellow dashed rectangle region marked in Fig. 3c is shown in Fig. 3d. One can see step-like Z-contrast intensity along the building units stacking direction, and the average intensity of 18R ( $I_{18\text{R}}$ ), 14H ( $I_{14\text{H}}$ ) and 24R ( $I_{24\text{R}}$ ) are measured to be 7.98, 7.45 and 7.08, respectively. The corresponding ratio of the experimental average Z-contrast intensity is 1:0.93:0.89. It is well known that Z-contrast intensity is basically proportional to the square of  $Z$ . Z-contrast intensity can be roughly

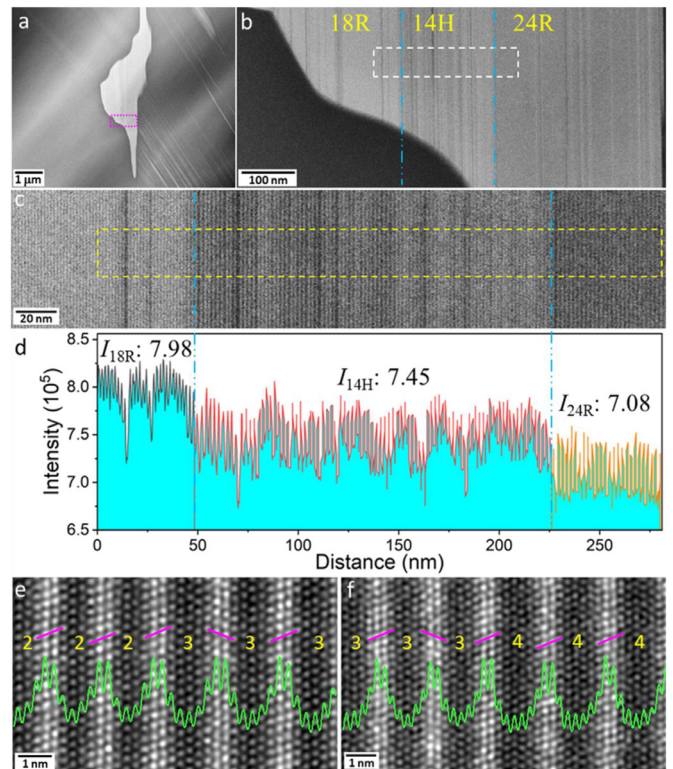


Fig. 3. HAADF-STEM images (a–c), the Z-contrast intensity profile (d) obtained from the yellow dashed frame region in (c), and the atomic-resolution HAADF-STEM images along with Z-contrast intensity profiles (e, f) around 18R/14H (e) and 14H/24R (f) interfaces. (b) and (c) are corresponding to the regions marked by pink rectangle in (a) and white rectangle in (b), respectively. Pink bars in (e, f) indicate AB'C'A-type stacking units.

estimated using the following formulae:

$$I = kZ^n \quad (1)$$

$$Z^n = \sum x_i Z_i^n \quad (2)$$

in which  $k$  is a constant,  $Z$  is atomic number,  $n = 1.7 \sim 2.0$ ,  $i$  is alloying element ( $i$  represents Mg, Ho and Cu in the present work),  $x_i$  and  $Z_i$  are atomic percent and atomic number of alloying element  $i$ , respectively. According to the TEM-EDS results of LPSO variants, the ratio of the Z-contrast intensity for 18R, 14H and 24R is estimated to be 1:0.93:0.88 by assuming  $n = 2$  in Eq. (1) and (2), providing a good agreement with the experimental ratio (1:0.93:0.89). This suggests that the average Z-contrast intensity in Fig. 3d can represent the average composition of LPSO variants, *i.e.* step-like Z-contrast intensity stands for step-like composition gradient. With the purpose of investigating the orientation relationships between three LPSO structural variants, the respective interfaces of 18R/14H and 14H/24R are characterized by atomic-resolution HAADF-STEM, as shown in Fig. 3e and f. The fully coherent interfaces are directly revealed at atomic scale, suggesting three LPSO structural variants originate from the same crystal nucleus during the solidification of alloy. Z-contrast intensity profiles of the relevant atomic columns are attached in Fig. 3e and f. It is significant that all the SESF layers with Cu/Ho

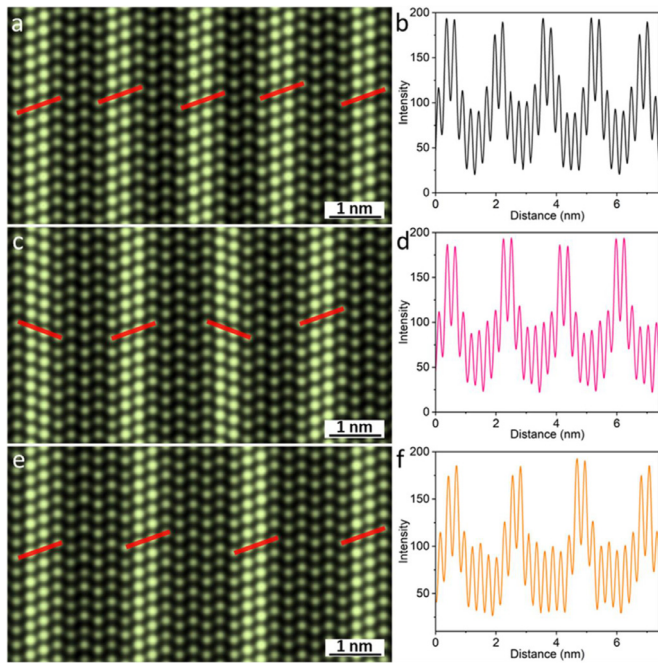


Fig. 4. Simulated HAADF-STEM images (a, c and e) along  $[11\bar{2}0]_{\text{hcp}}$  and the corresponding intensity profiles (b, d and f) along the stacking direction. Red bars in (a, c and e) indicate AB'C'A-type stacking units. (a, b), (c, d) and (e, f) are corresponding to 18R, 14H and 24R LPSO phases, respectively (For interpretation of the references to color in this figure, the reader is referred to the web version of this article.).

segregation exhibit almost identical intensity regardless of the type of LPSO phases, meaning that the chemical compositions of SESFs in all the LPSO phases are equivalent in the present alloy. In other words, and the chemical compositions of LPSO phases could vary mainly depending on the number of Mg layers sandwiched between adjacent SESFs [17]. It is pointed out that the different features of Z-contrast intensity profiles between Fig. 3d and (e, f) can be attributed to the different magnification of the obtained HAADF-STEM images.

The above experimental results can be also supported by the relevant HAADF-STEM simulations. Fig. 4a, c and e show the simulated atomic-resolution HAADF-STEM images of 18R, 14H and 24R LPSO phases, respectively, which are generated by using Dr. Probe [43] based on the experimental compositions of these LPSO variants. The structure features such as the shear direction of AB'C'A-type stacking units (indicated by red bars) in the simulated results are in line with the experimental HAADF-STEM images shown in Fig. 2f–h. The corresponding Z-contrast intensity profiles shown in Fig. 4b, d and f suggest that the chemical compositions of SESFs in these LPSO variants are almost equivalent regardless of the type of LPSO phase, which is well consistent with the experimental results shown in Fig. 3. In addition, the ratio of the average intensity for simulated 18R, 14H and 24R LPSO phases is estimated to be 1:0.96:0.93, which conforms with the experimental trend and can also support the reasonability of step-like composition gradient presented in Fig. 3 to

a certain extent. It is worthwhile to note here that the present annular detector was set to the angle higher than 68 mrad, which is significantly larger than the beam convergence angle of 22 mrad. Therefore, the present Z-contrast is able to provide the ideal  $Z^2$ -dependent (i.e.,  $n = 2$  in Eq. (1) and (2)), as anticipated by the condition close to Rutherford scattering behavior.

The robust  $L1_2$ -type  $\text{TM}_6\text{RE}_8$  clusters distributed across the *fcc* building units are considered to be a key factor in governing the chemical composition and order degree in  $I_2$ -type LPSO phases. They are frequently observed in Mg-Zn-Y [20–23,26] and Mg-Al-Gd [31] alloys and generally indicated by distinctly diffuse streaks paralleling to  $c^*$  direction in the SAED patterns of  $[11\bar{2}0]_{\text{hcp}}$  and  $[1\bar{1}00]_{\text{hcp}}$  incidences. However, analogous diffraction features representing superlattice structure cannot be observed in  $[11\bar{2}0]_{\text{hcp}}$  SAED patterns for the present alloy, as shown in Fig. 2c–e, implying the inexistence of long-range order clusters. Taking the 24R LPSO phase as an example, the representative SAED pattern and atomic-resolution HAADF-STEM image viewed from  $[1\bar{1}00]_{\text{hcp}}$  zone axis are also obtained to further examine the  $L1_2$ -type  $\text{TM}_6\text{RE}_8$  clusters, respectively shown in Fig. 5a and b. As shown in Fig. 5a, although additional streaks are absent, some weak diffusion peaks are still displayed along  $c^*$  direction in the diffraction pattern. Further examination of atoms' characteristic in Fig. 5b reveals a certain amount of particular configurations (marked by yellow dotted frames) that are automatically selected using a template-matching procedure based on the cross-correlation evaluations of the local contrast variations [44], representing SRO clusters are actually existed along SFs. According to previous reports [20–26], they are reasonably identified as  $L1_2$ -type  $\text{Cu}_6\text{Ho}_8$  clusters, even though some of them are incomplete due to the relatively dilute concentrations of Cu/Ho. As presented in Fig. 5c, two striking diffusion peaks indicated by yellow arrows are displayed in the fast Fourier transformation (FFT) pattern obtained from Fig. 5b, working in concert with the features of diffraction pattern. Fig. 5d presents the inverse FFT pattern generated by masking diffuse peaks in the corresponding FFT pattern, in which the remarkable fringe contrast marked by white dotted frames can also vindicate the existence of SRO  $L1_2$ -type  $\text{Cu}_6\text{Ho}_8$  clusters. Additionally, the detailed atomic structure of the SRO  $L1_2$ -type  $\text{Cu}_6\text{Ho}_8$  cluster is shown in Fig. 5e, which is generated by averaging over the similar contrast regions marked by yellow dotted frames in Fig. 5b [44]. It is basically consistent with the configuration of the typical  $\text{Zn}_6\text{Y}_8$  cluster proposed in Mg-Zn-Y alloy [20], further supporting the formation of SRO  $L1_2$ -type  $\text{Cu}_6\text{Ho}_8$  clusters in the present alloy. Furthermore, STEM-EDS was performed to investigate the chemical feature of the 24R LPSO phase. The EDS mappings of Mg, Ho, Cu and Zr elements for the HAADF-STEM image (Fig. 5b) are presented in Fig. 5f, and the corresponding intensity profiles of the HAADF-STEM image and EDS mappings along the stacking direction are presented in Fig. 5g. The results indicated that Ho and Cu are sharply segregated in the two middle layers of the 4-layer SESFs, while the solute segregation in the two outer layers

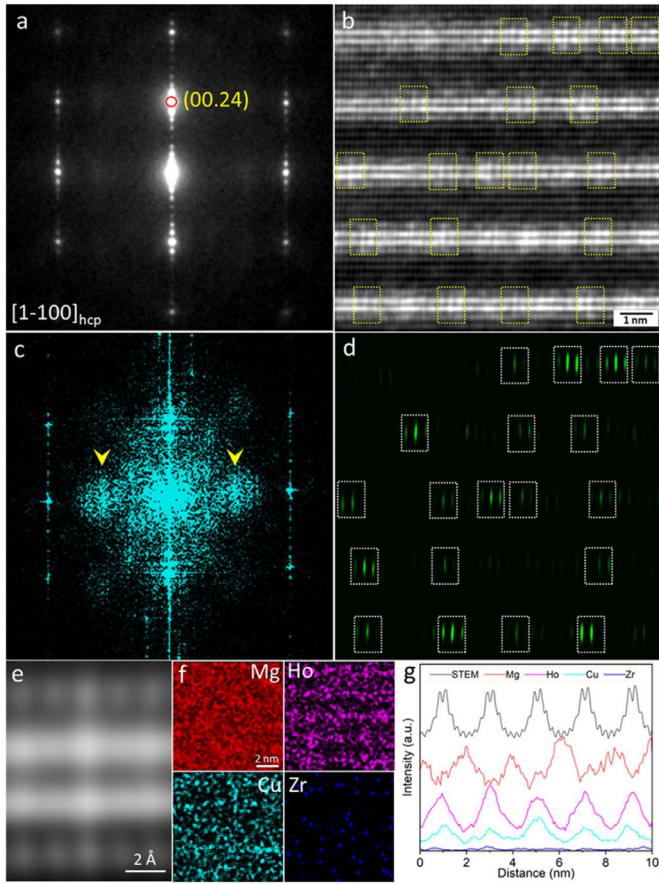


Fig. 5. SAED pattern (a) taken along  $[1\bar{1}00]_{\text{hcp}}$  zone axis, the corresponding atomic-resolution HAADF-STEM image (b), the FFT pattern (c) obtained from (b), and the inverse FFT patterns (d) generated by masking diffuse peaks indicated by yellow arrows in (c). The atomic structure of SRO  $L1_2$ -type  $\text{Cu}_6\text{Ho}_8$  cluster (e) generated by averaging over the similar contrast regions marked by yellow dotted frames in (b). The EDS mappings (f) for the HAADF-STEM image shown in (b), and the corresponding intensity profiles (g) of the HAADF-STEM image and EDS mappings along the stacking direction (For interpretation of the references to color in this figure, the reader is referred to the web version of this article.).

adjacent to Mg layers is relatively weak. Meanwhile, there is no distinct segregation of Zr in the LPSO phase, which is in accord with the results of SEM-EDS and TEM-EDS. It is further confirmed that the chemical distribution feature of LPSO phase fits in well with the Z-contrast characteristic of the corresponding HAADF-STEM image.

#### 4. Discussion

As described in the previous section (Table 1), the compositions of 18R, 14H and 24R LPSO phases marked by A, B and C in Fig. 1d were identified as  $\text{Mg}_{90.9}\text{Ho}_{4.9}\text{Cu}_{4.1}\text{Zr}_{0.1}$ ,  $\text{Mg}_{92.8}\text{Ho}_{4.1}\text{Cu}_{3.0}\text{Zr}_{0.1}$ , and  $\text{Mg}_{93.5}\text{Ho}_{3.7}\text{Cu}_{2.7}\text{Zr}_{0.1}$ , respectively. By comparison with Mg-Zn-Y alloys, the compositions of LPSO phases in the present alloy are very dilute, for instance, the composition of 18R LPSO structure was reported as  $\text{Mg}_{85.0}\text{Y}_{9.0}\text{Zn}_{6.0}$  [20]. It is particularly noteworthy that the ratios of Ho/Cu in three variants are very

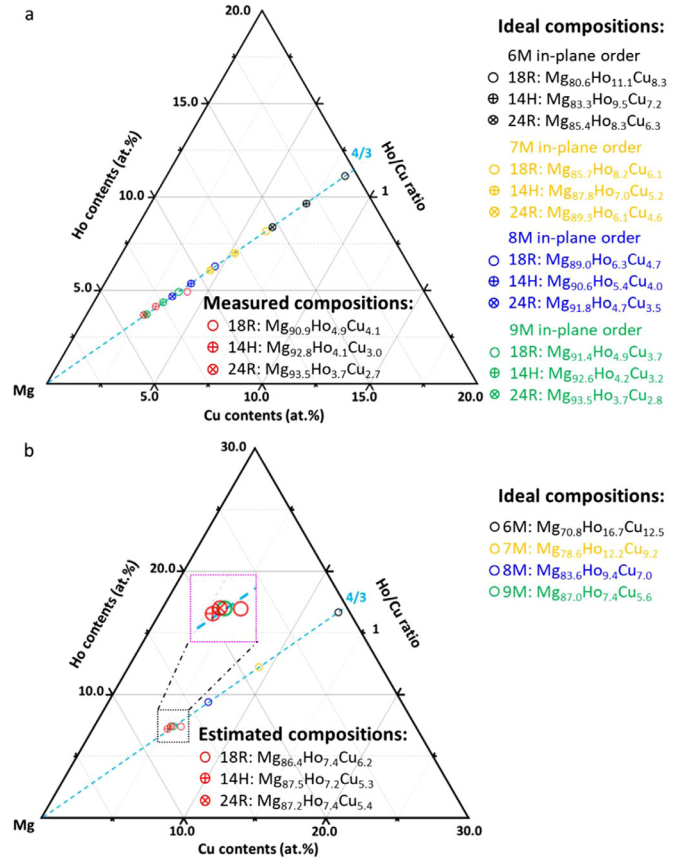


Fig. 6. Mg-Cu<sub>3</sub>Ho<sub>4</sub> cross-section schematics of LPSO phase (a) and SESF (b) around the Mg-rich corner in the Mg-Ho-Cu ternary phase diagram.

close to 4/3, as shown in Fig. 6a, even though their solute concentrations are indeed different. This is attributed to the nature of robust  $L1_2$ -type  $\text{Cu}_6\text{Ho}_8$  clusters in LPSO phase. As we mentioned already,  $\text{TM}_6\text{RE}_8$  clusters with 6M in-plane order were frequently observed in  $I_2$ -type LPSO phase for Mg-Zn-Y and Mg-Al-Gd alloys. The ideal stoichiometry compositions of corresponding 18R, 14H and 24R LPSO phases were estimated as  $\text{Mg}_{29}\text{TM}_3\text{RE}_4$ ,  $\text{Mg}_{35}\text{TM}_3\text{RE}_4$  and  $\text{Mg}_{41}\text{TM}_3\text{RE}_4$ , respectively [20,25–26]. Recently, relatively low-density  $\text{TM}_6\text{RE}_8$  clusters with 7M in-plane order were demonstrated in 12R LPSO phase for Mg-Ni-Y alloy [25], and the corresponding ideal stoichiometry compositions of 18R, 14H and 24R LPSO phases were expected to be  $\text{Mg}_{42}\text{TM}_3\text{RE}_4$ ,  $\text{Mg}_{301}\text{TM}_{18}\text{RE}_{24}$  and  $\text{Mg}_{175}\text{TM}_9\text{RE}_{12}$ , respectively. However, as shown in Fig. 6a, the measured compositions of LPSO phases in the present alloy are expanded into much more dilute regions, which cannot be matched by the ideal compositions of LPSO phases with 6M or 7M in-plane order clusters. This means that the SRO clusters in the present LPSO phases seem to stretch into much lower-density in-plane order. In this case, the ideal stoichiometry compositions of 18R, 14H and 24R LPSO phases with 8M and 9M in-plane order clusters were proposed. All the above ideal stoichiometry compositions (listed in Table 2) and the experimental compositions (listed in Table 1) in the present work are summarized in Fig. 6a. By the way, trace amounts of Zr

Table 2.  
The ideal chemical compositions of LPSO phases and SESFs.

LPSO phase (in-plane order)		Chemical formula	LPSO compositions (at.%)			SESF compositions (at.%)		
			Cu	Ho	Mg	Cu	Ho	Mg
6M	18R	Mg <sub>29</sub> Cu <sub>3</sub> RE <sub>4</sub>	8.3	11.1	Balance	12.5	16.7	Balance
	14H	Mg <sub>35</sub> Cu <sub>3</sub> RE <sub>4</sub>	7.2	9.5	Balance			
	24R	Mg <sub>41</sub> Cu <sub>3</sub> RE <sub>4</sub>	6.3	8.3	Balance			
7M	18R	Mg <sub>42</sub> Cu <sub>3</sub> RE <sub>4</sub>	6.1	8.2	Balance	9.2	12.2	Balance
	14H	Mg <sub>301</sub> Cu <sub>18</sub> RE <sub>24</sub>	5.2	7.0	Balance			
	24R	Mg <sub>175</sub> Cu <sub>9</sub> RE <sub>12</sub>	4.6	6.1	Balance			
8M	18R	Mg <sub>57</sub> Cu <sub>3</sub> RE <sub>4</sub>	4.7	6.3	Balance	7.0	9.4	Balance
	14H	Mg <sub>203</sub> Cu <sub>9</sub> RE <sub>12</sub>	4.0	5.4	Balance			
	24R	Mg <sub>235</sub> Cu <sub>9</sub> RE <sub>12</sub>	3.5	4.7	Balance			
9M	18R	Mg <sub>74</sub> Cu <sub>3</sub> RE <sub>4</sub>	3.7	4.9	Balance	5.6	7.4	Balance
	14H	Mg <sub>525</sub> Cu <sub>18</sub> RE <sub>24</sub>	3.2	4.2	Balance			
	24R	Mg <sub>101</sub> Cu <sub>3</sub> RE <sub>4</sub>	2.8	3.7	Balance			

is omitted in the ternary phase diagram. It is evident that the experimental compositions (red marks) for the present LPSO phases are very close to the ideal stoichiometry compositions (green marks) for LPSO phases of 9M in-plane order. The low cluster density provides a good explanation for the absence of distinct superlattice reflections paralleling to  $c^*$  direction in the SAED patterns for the present alloy. The occurrence of SRO in-plane robust  $L1_2$ -type  $TM_6RE_8$  clusters in the extraordinarily dilute Mg-Ho-Cu alloy supports that they do play an important role in LPSO phase formation. Assuming that the Mg layers sandwiched between adjacent SESFs contain no Cu/Ho solutes, the compositions of SESFs in 18R, 14H and 24R LPSO phases are estimated to be  $Mg_{86.4}Ho_{7.4}Cu_{6.2}$ ,  $Mg_{87.5}Ho_{7.2}Cu_{5.3}$ , and  $Mg_{87.2}Ho_{7.4}Cu_{5.4}$ , respectively. Similarly, the SESF compositions in ideal stoichiometric LPSO phases of 6M, 7M, 8M and 9M in-plane order are estimated to be  $Mg_{70.8}Ho_{16.7}Cu_{12.5}$ ,  $Mg_{78.6}Ho_{12.2}Cu_{9.2}$ ,  $Mg_{83.6}Ho_{9.4}Cu_{7.0}$ , and  $Mg_{87.0}Ho_{7.4}Cu_{5.6}$ , respectively. The SESFs compositions estimated from both the experimental and ideal compositions are summarized in Fig. 6b, in which the pink dashed rectangle region is enlarged from the black dashed rectangle region. It is obvious that the ideal composition of 9M in-plane order SESF can match well with the estimated values based on the experimental results. This further demonstrates that the SRO clusters in the present LPSO phases are 9M in-plane order. In addition, the results provide direct evidence for the equivalent SESF compositions in all the LPSO phases inferred from the identical  $Z$ -contrast intensity features shown in Fig. 3e and f.

## 5. Conclusion

The microstructures of as-cast  $Mg_{97.49}Ho_{1.99}Cu_{0.43}Zr_{0.09}$  alloy have been systematically characterized. The coherent LPSO structural variants (18R, 14H and 24R) along step-like composition gradient were identified at atomic scale in a blocky phase distributed at grain boundary. The robust SRO  $L1_2$ -type  $Cu_6Ho_8$  clusters embedded across the  $I_2$ -type SFs were revealed in the very dilute Mg-Ho-Cu alloy, directly indicating that SRO in-plane  $L1_2$ -type  $TM_6RE_8$  clusters can be extended into much more dilute composition regions bounded

along the fixed TM/RE ratio of 3/4. It is important that the order degree of SRO  $L1_2$ -type  $Cu_6Ho_8$  clusters was identified as 9M in-plane order, which is remarkably lower than frequently reported 6M and 7M in-plane order in traditional ternary Mg-TM/Al-RE alloys. Furthermore, in the present alloy, the chemical compositions of SESFs in these LPSO variants are equivalent regardless of the type of LPSO phases, which are almost identical with the ideal SESF composition of 9M in-plane order. The results further support the viewpoint that robust  $L1_2$ -type  $TM_6RE_8$  clusters play an important role in governing LPSO phase formation.

## Declaration of Competing Interest

There is no conflict of interest.

## Acknowledgments

This work was supported by JSPS KAKENHI for Scientific Research on Innovative Areas “Materials Science of a Millefeuille Structure (Grant Nos. JP18H05475, JP18H05479)”, and “Nanotechnology Platform” of the MEXT, Japan. K.G. was supported by Grant-in-Aid for JSPS Fellows (JP19F19775), and the Open Funds of the State Key Laboratory of Rare Earth Resource Utilization (RERU2020012). The authors would like to thank Prof. Qiang Yang and Prof. Jian Meng of the State Key Laboratory of Rare Earth Resource Utilization, Chinese Academy of Sciences, for providing experimental samples.

## References

- [1] S. Sandlöbes, S. Zaefferer, I. Schestakow, S. Yi, R. Gonzalez-Martinez, *Acta Mater.* 59 (2011) 429–439.
- [2] Y. Chino, M. Kado, M. Mabuchi, *Acta Mater.* 56 (2008) 387–394.
- [3] Y. Yang, X.M. Xiong, J. Chen, X.D. Peng, D.L. Chen, F.S. Pan, *J. Magnes. Alloy.* 9 (2021) 705–747.
- [4] J.F. Song, J. She, D.L. Chen, F.S. Pan, *J. Magnes. Alloy.* 8 (2020) 1–41.
- [5] K. Guan, F.Z. Meng, P.F. Qin, Q. Yang, D.D. Zhang, B.S. Li, W. Sun, S.H. Lv, Y.D. Huang, N. Hort, J. Meng, *J. Mater. Sci. Technol.* 35 (2019) 1368–1377.

- [6] E. Abe, Y. Kawamura, K. Hayashi, A. Inoue, *Acta Mater* 50 (2002) 3845–3857.
- [7] X.H. Shao, Z.Q. Yang, X.L. Ma, *Acta Mater.* 58 (2010) 4760–4771.
- [8] K. Hagihara, Z. Li, M. Yamasaki, Y. Kawamura, T. Nakano, *Acta Mater.* 163 (2019) 226–239.
- [9] D. Egusa, M. Yamasaki, Y. Kawamura, E. Abe, *Mater. Trans.* 54 (2013) 698–702.
- [10] D. Egusa, K. Inoue, Y. Nagai, E. Abe, *Mater. Charact.* 177 (2021) 111153.
- [11] Q. Yang, S.H. Lv, Z.X. Yan, X.R. Hua, X. Qiu, J. Meng, *Mater. Des.* 201 (2021) 109482.
- [12] Y. Kawamura, K. Hayashi, A. Inoue, T. Masumoto, *Mater. Trans.* 42 (2001) 1172–1176.
- [13] J.S. Xie, J.H. Zhang, Z.H. You, S.J. Liu, K. Guan, R.Z. Wu, J. Wang, J. Feng, *J. Magnes. Alloy.* 9 (2021) 41–56.
- [14] J.H. Zhang, S.J. Liu, R.Z. Wu, L.G. Hou, M.L. Zhang, *J. Magnes. Alloy.* 6 (2018) 277–291.
- [15] K. Guan, R. Ma, J.H. Zhang, R.Z. Wu, Q. Yang, J. Meng, *J. Magnes. Alloy.* 9 (2021) 1098–1109.
- [16] K. Guan, B.S. Li, Q. Yang, X. Qiu, Z. Tian, D.D. Zhang, D.P. Zhang, X.D. Niu, W. Sun, X.J. Liu, J. Meng, *J. Alloy. Compd.* 735 (2018) 1737–1749.
- [17] E. Abe, A. Ono, T. Itoi, M. Yamasaki, Y. Kawamura, *Philos. Mag. Lett.* 91 (2011) 609–696.
- [18] Y.M. Zhu, A.J. Morton, J.F. Nie, *Acta Mater.* 58 (2010) 2936–2947.
- [19] Y.M. Zhu, A.J. Morton, J.F. Nie, *Acta Mater.* 60 (2012) 6562–6572.
- [20] D. Egusa, E. Abe, *Acta Mater.* 60 (2012) 166–178.
- [21] T. Nishioka, Y. Yamamoto, K. Kimura, K. Hagihara, H. Izuno, N. Happo, S. Hosokawa, E. Abe, M. Suzuki, T. Matsushita, K. Hayashi, *Materialia* 3 (2018) 256–259.
- [22] M. Itakura, M. Yamaguchi, D. Egusa, E. Abe, *Acta Mater.* 203 (2021) 116491.
- [23] K. Kishida, K. Nagai, A. Matsumoto, A. Yasuhara, H. Inui, *Acta Mater.* 99 (2015) 228–239.
- [24] C. Liu, Y. Zhu, Q. Luo, B. Liu, Q. Gu, Q. Li, *J. Mater. Sci. Technol.* 34 (2018) 2235–2239.
- [25] K. Yamashita, T. Itoi, M. Yamasaki, Y. Kawamura, E. Abe, *J. Alloy. Compd.* 788 (2019) 277–282.
- [26] M. Yamasaki, M. Matsushita, K. Hagihara, H. Izuno, E. Abe, Y. Kawamura, *Scr. Mater.* 78–79 (2014) 13–16.
- [27] Y. Kawamura, T. Kasahara, S. Izumi, M. Yamasaki, *Scr. Mater.* 55 (2006) 453–456.
- [28] Y. Kawamura, M. Yamasaki, *Mater. Trans.* 48 (2007) 2986–2992.
- [29] M. Egami, I. Ohnuma, M. Enoki, H. Ohtani, E. Abe, *Mater. Trans.* 61 (2020) 839–848.
- [30] M. Egami, I. Ohnuma, M. Enoki, H. Ohtani, E. Abe, *Mater. Des.* 188 (2020) 108452.
- [31] H. Yokobayashi, K. Kishida, H. Inui, M. Yamasaki, Y. Kawamura, *Acta Mater.* 59 (2011) 7287–7299.
- [32] D. Egusa, K. Kawaguchi, E. Abe, *Front. Mater.* 6 (2019) 266.
- [33] H. Okuda, H. Tanaka, T. Shiratake, M. Yamasaki, Y. Kawamura, *Acta Mater.* 118 (2016) 95–99.
- [34] H. Okuda, M. Yamasaki, Y. Kawamura, *Scr. Mater.* 139 (2017) 26–29.
- [35] S. Hosokawa, J.R. Stellhorn, B. Paulus, K. Maruyama, K. Kobayashi, H. Okuda, M. Yamasaki, Y. Kawamura, H. Sato, *J. Alloy. Compd.* 764 (2018) 431–436.
- [36] H. Kimizuka, M. Fronzi, S. Ogata, *Scr. Mater.* 69 (2013) 594–597.
- [37] H. Kimizuka, S. Kurokawa, A. Yamaguchi, A. Sakai, S. Ogata, *Sci. Rep.* 4 (2014) 7318.
- [38] S.B. Mi, Q.Q. Jin, *Scr. Mater.* 68 (2013) 635–638.
- [39] K. Guan, M. Egami, D. Egusa, H. Kimizuka, M. Yamasaki, Y. Kawamura, E. Abe, *Scr. Mater.* 207 (2022) 114282.
- [40] S.H. Lv, X.L. Lv, F.Z. Meng, Y.W. Li, Q. Duan, Q. Yang, *J. Alloy. Compd.* 774 (2019) 926–938.
- [41] L. Zhang, J.H. Zhang, C. Xu, Y.B. Jing, J.P. Zhuang, R.Z. Wu, M.L. Zhang, *Mater. Lett.* 133 (2014) 158–162.
- [42] J.E. Saal, C. Wolverton, *Acta Mater.* 68 (2014) 325–338.
- [43] J. Barthel, *Ultramicroscopy* 193 (2018) 1–11.
- [44] M. Egami, E. Abe, *Scr. Mater.* 98 (2015) 64–67.